Exp. Theo. NANOTECHNOLOGY 10 (2026) 1565-1578 https://doi.org/10.56053/10.3.1565

Analysis of nuclear deformation properties for even–even Ne isotopes using Hartree–Fock and Bardeen–Cooper–Schrieffer theory

Saja H. Mohammed[1*], *R. T. Mahdi*[2], *Zainab K. Nasser Allah*[1]

[1]Department of Physics, College of Science, Al-Nahrain University, Jadiriya, Baghdad, Iraq
[2]Department of Physics, College of Science for Women, University of Baghdad, Jadiriya, Baghdad, Iraq
[*]) Email: saja.hazim@nahrainuniv.edu.iq

Received 16/4/2026, *Received in revised form* 23/5/2026, *Accepted* 2/6/2026, *Published* 15/7/2026

The deformation properties of even–even $^{24–30}$Ne isotopes are studied within the self-consistent Hartree–Fock plus Bardeen–Cooper–Schrieffer (HF+BCS) Theory using the Skyrme (SLy5) functional. Axially constrained calculations are performed to construct potential energy curves (PECs) as functions of the quadrupole deformation parameter β_2, enabling an analysis of shape evolution and shell effects nearby the $N = 20$ region. The results indicate a transition from a weakly deformed configuration in ^{24}Ne to a stable prolate shape in ^{26}Ne, followed by shape coexistence in ^{28}Ne and a near-spherical ground state in ^{30}Ne. Calculated binding energy and deformation parameters agree closely with experimental data. This research shows that the SLy5 functional within the HF+BCS method accurately portrays deformation systematics in neutron-rich nuclei, particularly the effects of shell-driven collectivity and neutron-driven shell stabilization.

Keywords: Nuclear deformation; Hartree–Fock method; BCS pairing; neon isotopes; shape coexistence.

1. INTRODUCTION

Nanotechnology presents new insights into potential nuclear uses and is a revolution in our knowledge of materials at the atomic scale. Theoretical models can more accurately depict nuclear interactions

and subatomic dynamics by manipulating nanostructures [1]. Nuclear deformation is a fundamental collecting events phenomenon in nuclei and plays an essential role in determining these nuclei both its intrinsic structure and excitation dynamics. A charge radius and probabilities of electromagnetic transition are features that are highly responsive to the departure from spherical symmetry. Even-even nuclei, in particular, represent an important testing ground to study the interplay between pairing correlations and the mean-field owing to the absence of unpaired nucleons, which makes the collective effects easier to observe.

Light nuclei in the sd-shell regions have different shapes, from round to elongated, which are affected by small changes in the number of neutrons or in which shells are filled. These changes occur in neutron-rich neon isotopes near the "island of inversion" at number of neutron = 20, where the usual shell closure ineffective. Configurations from the fp shell have energy similar to the standard sd configurations. Experimental and theoretical studies have shown that these nuclei have quadrupole collectivity; they also display shape coexistence. This illustrates how structure, pairing correlations, and forces that cause deformation all work together. In sd-shell nuclei, these have a connection, which we will try to understand by studying neutron rich neon isotopes. The structures and forces of deformation define the shapes of these nuclei. The shapes of effective nucleon densities change suddenly with either neutron number or shell occupancy [2–5]. By examining the distribution of nucleons outside the closed shell, this deformation can be explained. In microscopic systems, the many-body problem, despite the relatively small number of particles, makes it impossible to obtain exact solutions to the Schrödinger equation. Consequently, theories and methods have evolved to reduce the situation to a single-particle problem in order to facilitate an approximate solution for these systems. These estimates, referred to as mean-field techniques [6], are an important method for determining the structure of a nuclear system. They rely on the finding that, to a decent approximation, distinct nucleons function within the nucleus as independent particles situated in an average potential formed by other nucleons. The (HF) approximation [7,8] is a mean-field theory that can be used for many-body systems. Pairing correlations are a principal residual interaction in the atomic nucleus, especially in the open-shell systems. The pairing forces between nucleons are caused by the attractive interaction between identical nucleons in time-reversed states near the Fermi surface(F_S). It produces staggering of binding energies and other phenomena exhibiting collective motion [9]. In practical calculations of nuclear structures, the (BCS) theory, in conjunction with self-consistent mean-field methods, leads to HF+BCS schemes. In the mean field (MF) approximation, this model determines the single-particle spectrum whereas the BCS equations account for the pairing correlations of the nucleons, which is situated close to the FS. This method is commonly utilized when analyzing axially deformed systems within the Skyrme energy-density functional convention and provides good outcomes for even-even nuclei [10]. Pairing correlations make a large contribution to nuclear deformation properties by reducing shell effects and smoothing potential energy surfaces. Strong pairing tends to favor collective deformation and shape coexistence, whereas weak pairing enhances shell closures and stabilizes spherical configurations near magic numbers [11]. In practical nuclear structure calculations BCS formalism are usually combined with self-consistent (MF) ones to form the HF+BCS approach. Within this model, the MF determines the single-particle spectrum, while the BCS equations account for the pairing correlations at the Fermi surface. This technique is especially ideal for even-even nuclei [12]. Within self-consistent (MF) approaches such as HF+BCS, neon isotopes show well-developed minima in their potential energy surfaces at nonzero quadrupole deformation parameter β_2. The depth of these minima increases with neutron number, indicating enhanced collectivity and shape stability in neutron-rich systems [13]. The experimental and theoretical investigations of neutron-rich isotopes ^{30}Ne and ^{32}Ne are indicating a breakdown of the traditional magic number N = 20 for those nuclei that are known to belong to the so-called island of inversion,

where the ground state is dominated by configurations of intruders from pf shell. Consequently, while the standard shell model forecasts a spherical shape for these isotopes, they actually undergo significant prolate deformations [14]. These modifications of the nucleon–nucleon interactions and the principles of structural evolution in nuclei cause changes in the nuclear parameters such as radii, charge distributions, and density profiles. They also result in the phenomenon of nuclear deformation [15,16]. This study combines new techniques and traditional models to perform precise nuclear structure investigations. The Skyrme (SLy5) functional is used in an HF+BCS study of the even–even isotopes $^{24-30}$Ne. The functional equalizes the overall features of a nucleus and explains the shell effects. We attempt to explain the evolution of nuclear shapes with increasing neutron numbers and examine neutron-induced deformation in the $N = 20$ region. We focus on shape coexistence and compare our results using the experimental data that is currently available and more advanced theories. We consider potential energy surfaces, equilibrium deformation parameters, binding energies, densities, and the aforementioned properties at several deformation values.

2. THEORETICAL FRAMEWORK

2.1 Hartree–Fock calculations

Pairing correlations have been incorporated into the investigation of transitional behaviors in nuclear density distributions using the Skyrme force framework. Nuclear structure and the development of nuclear forms are investigated using self-consistent mean-field HF+BCS computations. The HF approach is particularly effective for predicting single-particle levels and total binding energies in closed-shell nuclei. Furthermore, the Skyrme HF method proves useful because of its central character and the zero-range nature of its interactions. The nucleus exhibits quadrupole collectivity as many-body system, which reflects the mean-field deformation. This collective behavior is quantified through the expectation value of the quadrupole operator $\hat{Q}$. The fundamental component of MF theory is a collection of single-particle wave functions ψ_α, which are associated with a fractional occupation amplitude v_α, corresponding to a specific single-particle state α [19]:

$$\left\{ {}^{\psi_\alpha}, v_\alpha, \alpha = 1, \dots, \Omega \right\} \tag{1}$$

where the occupancy amplitudes v_α are confined to the interval $0 \leq v_\alpha \leq 1$, Ω indicates the size of the active single-particle space. The complementary non-occupation amplitude is well-defined by $u_\alpha = \sqrt{1 - v_\alpha^2}$. In the HF+BCS framework, nuclear ground state is approximated by BCS many-body wave function,

$$|\Phi\rangle = \prod_{\alpha>0} (u_\alpha + v_\alpha \hat{a}_\alpha^+ \hat{a}_{\bar{\alpha}}^+)|0\rangle \tag{2}$$

particle's vacuum state is represented by $^{|0\rangle}$, $\hat{a}_\alpha^+$ is the creation operator for a fermion in state $^{\psi_\alpha}$, $\bar{\alpha}$ is the time-reversed counterpart for state α..

2.2 Currents and local densities

The Skyrme energy-density functional depends explicitly on a limited set of local densities, namely, the particle density ρ_q, kinetic density τ_q, spin–orbit density J_q, and pairing density ξ_q, all of which are constructed from the HF single-particle wave functions and BCS occupation probabilities as follows:

$$\rho_q(\boldsymbol{r}) = \sum_{\alpha \in q} \sum_s v_\alpha^2 |\psi_\alpha(\boldsymbol{r}, s)|^2,$$

$$\boldsymbol{J}_q(\boldsymbol{r}) = -\mathrm{i}\sum_{\alpha\in q}\sum_{ss'} v_\alpha^2 \psi_\alpha^*(\boldsymbol{r},s)\nabla\times\sigma_{ss'}\psi_\alpha(\boldsymbol{r},s') \quad ,$$

$$\tau_q(\boldsymbol{r}) = \sum_{\alpha\in q}\ \sum_s\ v_\alpha^2|\nabla\psi_\alpha(\boldsymbol{r},s)|^2 \tag{3}$$

$$\xi_q(\mathbf{r}) = \sum_{\alpha\in q}\ \sum_s\ w_\alpha u_\alpha v_\alpha \psi_{\bar{\alpha}}(\mathbf{r},s)\psi_\alpha(\mathbf{r},s) \tag{4}$$

Here, q designates the nucleon type, $q = \mathrm{p}$ representing protons, $q = \mathrm{n}$ neutrons, and w_α indicates a soft cutoff in the pairing space. The spinor component and total local density $\rho = \rho_p + \rho_n$ are indicated by the variable $s \in \pm 1$.

2.3 Skyrme energy-density functional

The Skyrme force, a density-dependent effective interaction, defines the Skyrme HF approximation [19]:

$$\begin{aligned} V_{\mathrm{Sk}} = {} & t_0\left(1+x_0\hat{P}_\sigma\right)\delta(\mathbf{r}_{12}) \\ & +\tfrac{t_3}{6}\left(1+x_3\hat{P}_\sigma\right)\rho^\gamma(\mathbf{r}_1)\delta(\mathbf{r}_{12}) \\ & +\tfrac{t_1}{2}\left(1+x_1\hat{P}_\sigma\right)\left(\delta(\mathbf{r}_{12})\hat{\boldsymbol{k}}^2+\hat{\boldsymbol{k}}^2\delta(\mathbf{r}_{12})\right) \\ & +t_2\left(1+x_2\hat{P}_\sigma\right)\hat{\boldsymbol{k}}\delta(\mathbf{r}_{12})\hat{\boldsymbol{k}} \\ & -\mathrm{i}t_4\delta(\mathbf{r}_{12})(\hat{\boldsymbol{\sigma}}+\hat{\boldsymbol{\sigma}}')\cdot\left(\hat{\boldsymbol{k}}'\times\hat{\boldsymbol{k}}\right) \end{aligned} \tag{5}$$

where $\hat{P}_\sigma = \frac{1}{2}\,(1+(\hat{\boldsymbol{\sigma}}_1\hat{\boldsymbol{\sigma}}_2))$ is the spin-exchange operator, $\mathbf{r}_{12} = \mathbf{r}_1 - \mathbf{r}_2$, and the momentum operator is $\hat{\boldsymbol{k}} = -\mathrm{i}\nabla$ divided by $\hbar$. However, this is only necessary to enable the operation of a Skyrme interaction generator $\langle\Phi|V_{\mathrm{Sk}}|\Phi\rangle$, which serves as an effective interaction within the energy-density functional framework [17].

The HF+BCS equations are obtained by minimizing the total energy functional E_{tot} with respect to the single-particle wave functions and the BCS occupation amplitudes, under a particle-number constraint. The total energy, which is the starting point for the treatment, is constructed as follows:

$$E_{\mathrm{tot}} = T + E_{\mathrm{Sk}} + E_{\mathrm{Coulomb}} + E_{\mathrm{pair}} + E_{\mathrm{cm}} \tag{6}$$

where kinetic energy is given by

$$T = \sum_4 \frac{\hbar^2}{2m_4}\int dV_{t_4} \tag{7}$$

Skyrme forces are a popular interaction model and are employed in the code [20].

Skyrme energy is given as

$$\begin{aligned} E_{\mathrm{Sk}} = {} & \int dV\left(\tfrac{b_o}{2}\rho^2 - \tfrac{\acute{b}_o}{2}\textstyle\sum_q\ p_q^2\right) \\ & +\int dV\left(\tfrac{b_3}{3}\rho^{\gamma+2} - \tfrac{\acute{b}_3}{3}\rho^\gamma\textstyle\sum_{\mathrm{q}}\ p_q^2\right) \\ & +\int dV\left(-\tfrac{b_2}{2}\rho\Delta_p + \tfrac{\acute{b}_2}{2}\textstyle\sum_q\ p_q\Delta p_q\right) \\ & +\int dV\left(b_{1pt} - \acute{b}_1\textstyle\sum_q\ p_q t_q\right) \\ & -\int dV\left(b_4 e^{\nabla}.J^- \acute{b}_4\textstyle\sum_q\ p_{\mathrm{q}}\nabla.J_4\right) \\ & -\int dV\left(cJ^2 - \acute{C}_1\textstyle\sum_q\ J_q^2\right). \end{aligned} \tag{8}$$

The Coulomb energy is

$$E_C = \frac{e^2}{2}\int dV d\grave{V}\,\frac{p_p(\boldsymbol{r})p_p(\acute{r})}{|\boldsymbol{r}-\boldsymbol{r}|} - \int\ dv\,\frac{3e^2}{4}\left(\frac{3}{\pi}\right)^{\frac{1}{3}} p_p^{\frac{4}{3}}. \tag{9}$$

The pairing energy is

$$E_{\text{pair}} = \frac{1}{4}\sum_{q\in\{p,n\}} V_{\text{pair},\text{q}}\int\ \mathrm{d}V\left|\xi_q\right|^2\left[1-\frac{\rho}{\rho_{0,\text{ pair}}}\right] \tag{10}$$

where a volume element is represented by dV, and e^2 = 1.43989 MeV·fm. second component of the Coulomb energy is the exchange term in the Slater approximation.

In addition to the Skyrme forces, pairing interactions can be involved within the BCS [19]. A density-dependent pairing functional is used. This is derived from a density-dependent delta interaction, $V_{\text{pair}} \times \delta(1-12)[1-\rho(r)/\rho_{0,\text{pair}}]$ [21]. The balance between surface pairing and volume is regulated by the parameter $\rho_{0,\text{pair}}$ The electric quadrupole moment indicates nuclear deformation. This is the departure from spherical symmetry with respect to the center of mass. Consequently, the most significant moments are the center of mass moments [22]. There are two approaches that can be used to apply the center-of-mass correction E_{cm}, which eliminates the spurious energy resulting from the center-of-mass motion in the MF [23]:

$$E_{\text{cm}} = E_{\text{cm}}^{(\text{full})} = \frac{\left(\hat{\boldsymbol{P}}_{\text{cm}}^2\right)}{2\text{M}}, \hat{\boldsymbol{P}}_{\text{cm}} = \sum\ {}_{n=1}^{1}\,\boldsymbol{p}_n \tag{11}$$

$$E_{\text{cm}} = E_{\text{cm}}^{(\text{diag})} = \frac{\left(\sum_{\text{n=1}}^{\text{A}},\hat{p}_{\text{n}}^2\right)}{2\text{M}} \tag{12}$$

The expression for the Skyrme energy function in (5) is more effectively explained by the parameters b_0, b_0', ..., b_4'. These are substitutes for the traditional Skyrme operators t_1 and x_1, through [24]

$$b_0 = t_0\left(1+\frac{1}{2}x_0\right)$$

$$b_0' = t_0\left(\frac{1}{2}+x_0\right)$$

$$b_1 = \frac{1}{4}\left[\iota_1\left(1+\frac{1}{2}x_1\right)+\iota_2\left(1+\frac{1}{2}x_2\right)\right]$$

$$b_1' = \frac{1}{4}\left[t_1\left(\frac{1}{2}+x_1\right)-t_2\left(\frac{1}{2}+x_2\right)\right]$$

$$b_2 = \frac{1}{8}\left[3t_1\left(1+\frac{1}{2}x_1\right)-t_2\left(1+\frac{1}{2}x_2\right)\right]$$

$$b_2' = \frac{1}{8}\left[3t_1\left(\frac{1}{2}+x_1\right)+t_2\left(\frac{1}{2}+x_2\right)\right]$$

$$b_3 = \frac{1}{4}l_3\left(1+\frac{1}{2}x_3\right)$$

$$b_3' = \frac{1}{4}t_3\left(\frac{1}{2}+x_3\right)$$

$$b_4 = \frac{1}{2}t_4$$

$$c_1 = \eta_{tts}\frac{1}{16}(\iota_1 x_1+\iota_2 x_2)$$

$$c_1' = \pi tts \frac{1}{16}(t_1 - t_2) \tag{13}$$

where $b_4' = \frac{1}{2} t_4$ [23].

2.4 The coupled MF and BCS equations

The single-particle energies, the non-occupation amplitude u_a, and the pairing gaps that determine the equilibrium nuclear shapes are obtained by solving the coupled HF+BCS equations self-consistently. This results in [25, 26]

$$\left(\hat{h} + \frac{u_a}{t_a}\Delta(\boldsymbol{r})\right)\psi_a = \varepsilon_a \psi_a \tag{14}$$

$$\left(\varepsilon_\alpha - \epsilon_{F.q\alpha}\right)(u_\alpha^2 - v_\alpha^2) = \Delta_\alpha w_\alpha u_\alpha v_a \tag{15}$$

where $\hat{h}$ is the Hamiltonian operator, $\Delta(\boldsymbol{r})$ is the pairing potential (gap function), and $\epsilon_{F.q\alpha}$ is the Fermi energy. The HF single-particle Hamiltonian derived from the Skyrme functional takes the form [27];

$$\hat{h_{\mathrm{q}}} = U_{\mathrm{q}}(\boldsymbol{r}) - \nabla \cdot \left[B_{\mathrm{q}}(\boldsymbol{r})\nabla\right] + i\boldsymbol{W}_{\mathrm{q}} \cdot (\boldsymbol{\sigma} \times \nabla) \tag{16}$$

where $U_{\mathrm{q}}(\boldsymbol{r})$ is the local scalar potential, $-\nabla \cdot \left[B_{\mathrm{q}}(\boldsymbol{r})\nabla\right]$ represents the kinetic energy and the effective mass term, and $iW_q \cdot (\sigma \times \nabla)$ is the spin–orbit coupling term [28].

The pairing field (gap potential) is defined as [29]

$$\Delta_q(\boldsymbol{r}) = \frac{1}{2} V_{\mathrm{pair},q} \xi_q \left[1 - \frac{\rho}{\rho_{0,\,\mathrm{pair}}}\right] \tag{17}$$

and the pairing gap associated with a single-particle state α is [30]:

$$\Delta_\alpha = \int \mathrm{d}V |\psi_\alpha|^2 \Delta_{q_\alpha}(\boldsymbol{r}) \tag{18}$$

where the nucleon type linked to state α is q_α. The well-known Hartree–Fock–Bogolyubov (HFB) equations can be written as (14) and (15) [24]. Because of the gap potential's state-dependent contribution in (14) [25], their solution is fairly complicated. We agreement with the BCS approximation by omitting the term.

The gap equation (14) can be resolved to [31]

$$v_\alpha^2 = \frac{1}{2}\left(1 - \frac{\varepsilon_\alpha - \epsilon_{\mathrm{F},q_\alpha}}{\sqrt{\left(\varepsilon_\alpha - \epsilon_{\mathrm{F},q_\alpha}\right)^2 + w_\alpha \Delta_\alpha^2}}\right) \tag{19}$$

$$\Delta_\alpha = \frac{1}{2} V_{\mathrm{pair},\mathrm{q}_\alpha} \int \mathrm{d}V \psi_\alpha^+ \psi_\alpha \xi_{q_\alpha} \left[1 - \frac{\rho}{\rho_{0,\,\mathrm{pair}}}\right] \tag{20}$$

$$\epsilon_{\mathrm{F},q} : \sum_{\alpha \in q} v_\alpha^2 = N_q \tag{21}$$

The BCS gap potential $\Delta_q(r)$ and the average single-particle gap Δ_α are derived from the pairing interaction [32]:

$$v_\alpha^2 = \frac{1}{2}\left(1 - \frac{\varepsilon_\alpha - \varepsilon_{F,q}}{\sqrt{(\varepsilon_\alpha - \varepsilon_{F,q})^2 + \Delta_\alpha^2}}\right).$$

This equation determines the occupation probabilities based on the single-particle energy ε_α, the Fermi energy $\varepsilon_{F,q}$, and the pairing gap Δ_α

2.5 Density and multipole moments

The local nucleon density $p_q(r)$ is the next significant observable. The divergence from spherical symmetry around the mass of center, represented by the electric quadrupole moment, is known as nuclear deformation. Therefore, the most important moments are those in the center of mass:

$$\boldsymbol{R}_{\text{type}} = \frac{\int \mathrm{d}V \boldsymbol{r} \rho_{\text{type}}(\boldsymbol{r})}{\int \mathrm{d}V \rho_{\text{type}}(\boldsymbol{r})} \tag{22}$$

Here, ρ_{type} can be a proton density ρ_p , a neutron density ρ_n , an isovector density, an isoscalar density $\rho = \rho_p + \rho_n$, or the total density. $\rho_{T=1} = \frac{N}{A}\rho_p - \frac{Z}{A}\rho_n$

$$r_{\text{min, type}} = \sqrt{\frac{\int \mathrm{d}V (\boldsymbol{r} - \boldsymbol{R}_{\text{type}})^2 \rho_{\text{type}}(\boldsymbol{r})}{\int \mathrm{d}V \rho_{\text{type}}(\boldsymbol{r})}} \tag{23}$$

The spherical quadrupole moments can be used to quantify the anisotropic combinations:

$$Q_{2m,\text{type}} = \int dV r^2 \boldsymbol{Y}_{2m} \rho_{\text{type}}(\boldsymbol{r} - \boldsymbol{R}_{\text{type}}) \tag{24}$$

where Y_{2m} are the spherical harmonics and $r = |\mathbf{r}|$. Nonvanishing quadrupole moments are only permitted by axial symmetry when $m = 0$. They are usually expressed as dimensionless quadrupole moments:

$$\beta_{20} = \frac{4\pi}{3}\frac{Q_{20}}{AR^2}, R = R_0 A^{\frac{1}{3}}, R_0 = 1.2 \text{ fm} \tag{25}$$

where R is a radius similar to the nuclear diffraction radius. The quadrupole deformation parameter β_2 is extracted from the self-consistent density distribution obtained within the HF+BCS framework and is used to characterize the nuclear equilibrium shape.

Each field and wave function is represented on an axial grid. Axial and Cartesian coordinates relate to one another as follows:

$$r = \sqrt{X^2 + Y^2}, Z = Z \tag{26}$$

The axial coordinate r represents the separation from the symmetry axis. Examples of axially symmetric functions, meaning that they only depend on the r and z axes, are densities and potentials, both of which are displayed on a central grid:

$$r \leftrightarrow \{r_0, \dots, r_{N_r}\}, r_v = v\Delta r \tag{27}$$

$$z \leftrightarrow \{(z_{-N_z}, \dots, z_{-1}), z_0, \dots, z_{N_z}\}, z_v = v\Delta z \tag{28}$$

where the grid spacing is determined by the numerical parameters Δr and Δz. The full grid from $-Nz$ to $+Nz$ along the z-axis permits reflection-asymmetric nuclear configurations, or a grid from 0 for $+Nz$ can be used when reflection symmetry is present. Potentials and densities are symmetric functions $f(r,z)$ that may be expressed on the grid as $f(r_{vr}, z_{vz})$ [28].

A single particle's wave function has a more complicated composition that includes spin and rotational dependence. It can be represented as [22]

$$\psi_\alpha = \begin{pmatrix} \psi_\alpha^{(+)}(r_{v_r}, z_{v_z}) \exp(i m_\alpha \phi) \\ \psi_\alpha^{(-)}(r_{v_r}, z_{v_z}) \exp(i(m_\alpha + 1/2)\phi) \end{pmatrix} \tag{29}$$

where m_α denotes the z-component of the orbital angular momentum of the higher spin component, and $K_\alpha = m_\alpha + ½$ represents the z-component of the overall z angular momentum. The HF+BCS and HFB are mean-field approaches that mainly differ in their treatment of pairing correlations. The SkyAx code

utilizes the BCS approximation, which applies a simplified HFB formalism, and is most accurate for well-bound, even–even nuclei. In the regions around the drip lines, continuum effects start to become important and this HFB technique is more useful for a complete description of pairing but is also more complicated. The two methods can show pairing instability near closed shells but are limited in application because they assume axial symmetry and can only treat weakly bound states. The numerical accuracy of interaction scores depends on the grid parameters and the convergence standards. Also, large spatial volumes are needed for reasonable results for weakly bound nuclei.

3. RESULTS AND DISCUSSION

The analysis of Figure 1 indicates that the axially constrained HF-BCS calculations of even-even neon $^{24\text{-}30}$Ne reveal the PEC$_S$ as a function of the quadrupole deformation parameter β_2. The gradual evolution of the curves as the neutron number rises gives information about the balance between shell effects and quadrupole correlations just above the $N = 20$ region which are known to be very sensitive to shape-induced structural changes. The PEC of ^{24}Ne is a solitary, slight minimum at a minor oblate deformation. The gentle curvature near the minimum suggests a soft potential energy landscape, indicating that the nucleus fluctuates in form. Nuclei that exhibit moderate collective correlations are usually those that are not strong enough to stabilize a distinctly deformed ground state. The near-flat characteristic of the PEC does not indicate quadrupole coherence and is compatible with the more typical shell-correlation-induced partial limitation of deformation. In contrast, ^{26}Ne has a distinctly prolate minimum with more marked curvature. An enhancement of the PEC near this minimum shows the beginning of a stable quadrupole deformation. This shift may occur because neutron correlations are becoming important when valence neutrons fill orbitals which cause deformation. This induces quadrupole collectivity and reduces the overall energy via a collective motion common to all particles. The marked curvature shows a relatively stiff potential, which reflects a well-defined intrinsic shape and low shape variability. The PES of ^{28}Ne is much flatter than that of ^{26}Ne, showing two competing minima corresponding to oblate and prolate shapes with almost degenerate energies. Nuclei with this form always exhibit transitions to other forms and strong evidence for shape coexistence. The small energy disparity between the minima suggests considerable mixing of configurations, and many intrinsic shapes mix in low-energy excitations. This indicates the existence of a balance between these shell effects and quadrupole correlations which means that a quantitative account must go beyond mean field. This means mixture configuration or symmetry restoration must be used. Despite this, the HF+BCS framework captures the inherent softness and coexistence tendency at the mean-field level [29,30].

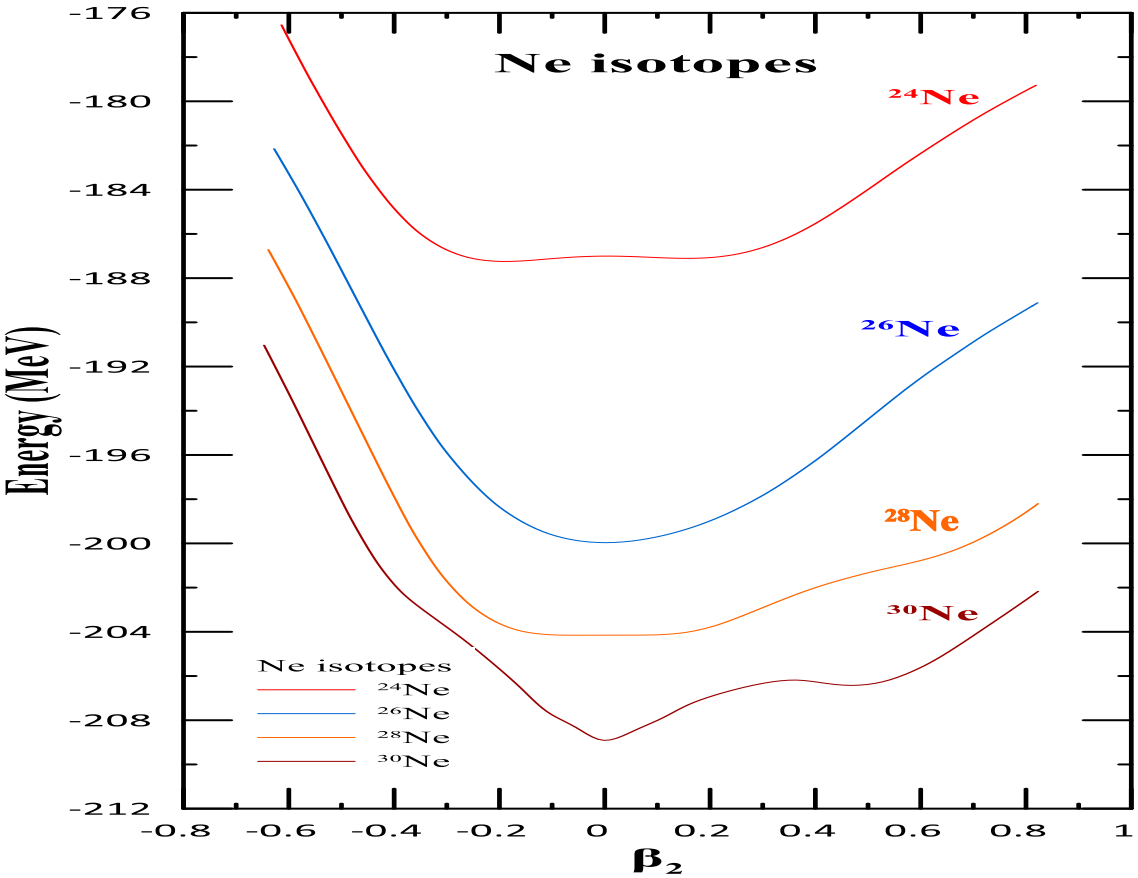

Figure 1 PECs of Ne isotopes as a function β_2.

In case of ^{30}Ne, the PEC has a minimum around $\beta_2 = 0$, and the curvature is steep, indicating almost a sphere. We see a more enhanced stabilizing effect from shell effects against collective quadrupole correlations. Under HF+BCS approximation, complete spherical symmetry enhancement due to shell stabilization will take place. Therefore, destabilizing deformation will also be smaller. Though more powerful methods that take into account additional dynamical correlations may provide more extensive deformation, the current results are completely compatible with the HF+BCS method's limitations and prediction range. The PECs in ^{24}Ne to ^{30}Ne exhibit a softer and milder deformation. This is followed by the development of strong, well-deformed, and transitional nuclei. The spherical stability then shows a resurgence. This regularity indicates the robustness of the HF+BCS methodology for the depiction of qualitative features of nuclear deformation, which is supplemented with convincing microscopic evidence for the competing effects of shell structure and quadrupole collectivity in the $N = 20$ region. Figures 2 to 5 show the PECs of the even–even neon isotopes $^{24–30}$Ne, along with their corresponding proton and neutron density distributions at stable deformations [31]. The density profiles validate the deformation patterns implied by the PECs and precise values given in Table 1 at microscopic level [32].

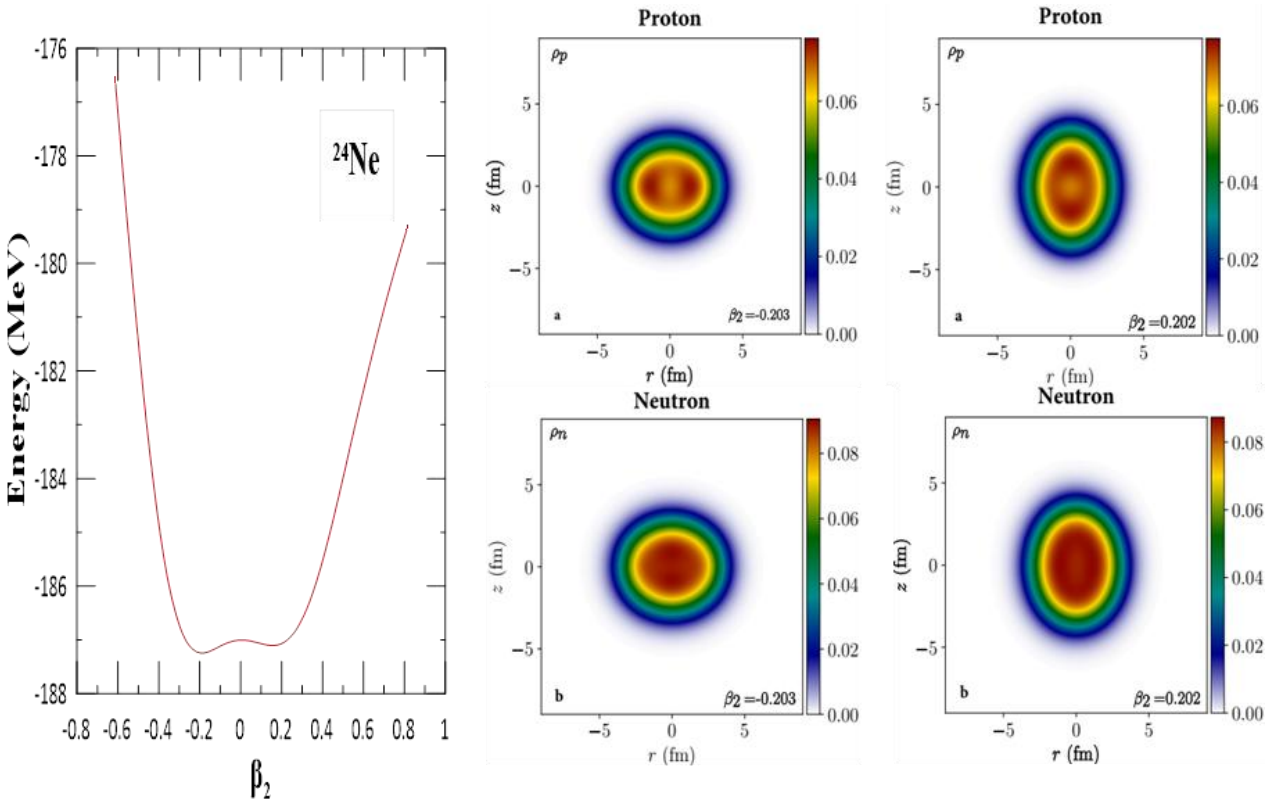

Figure 2 Left panel: PECs of ^{24}Ne as a function of β_2. Proton and neutron structure densities corresponding to the two local minima are shown on the right.

The PEC of ^{24}Ne exhibits a small minimum at a slight oblate deformation that is in agreement with the equilibrium value $\beta_2 = -0.05$ in Table 1. The densities of neutrons and protons are nearly spherical and slightly axially asymmetric. Similarity of the densities of protons and neutrons implies weak isoscalar quadrupole correlations and confirms small, dynamic deformation effects. The reduced binding energy in lighter isotopes indicates a lack of robust collective stabilization [33].

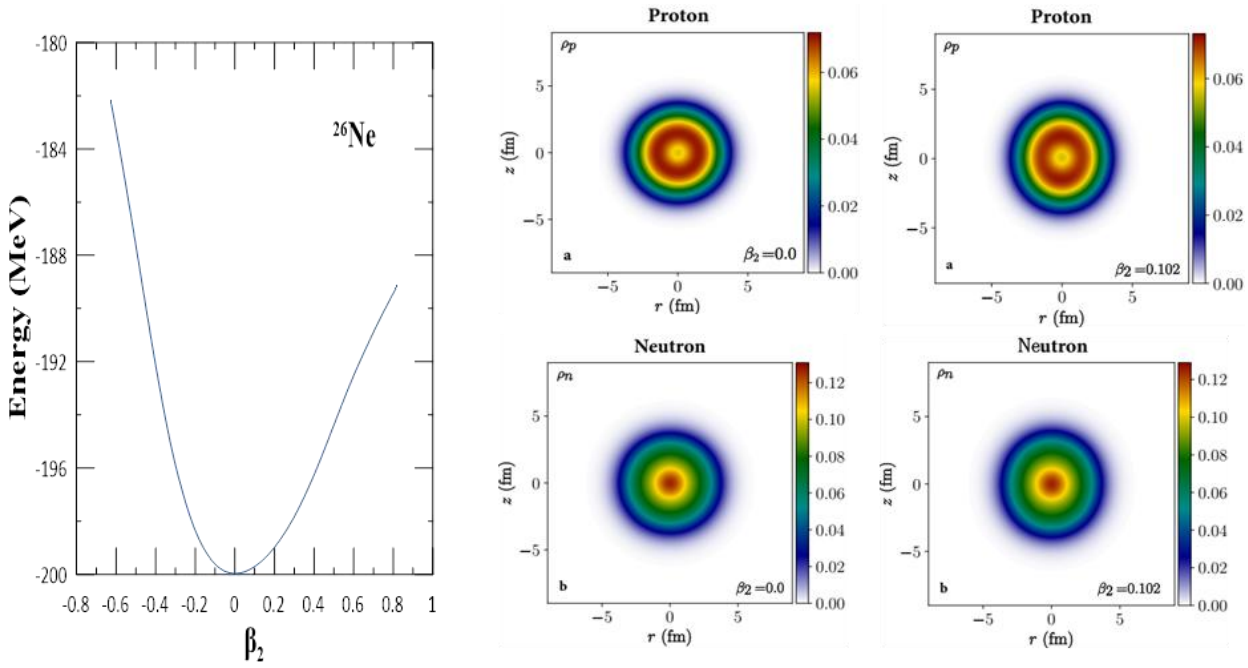

Figure 3 Left panel: PECs of ^{26}Ne as β_2. The proton and neutron structure densities corresponding to the two local minima are shown on the right.

In ^{26}Ne, the PEC shows a distinct prolate minimum consistent with the positive value of equilibrium deformation $\beta_2 = -0.10$. The corresponding density plots reveal a clear elongation along the symmetry axis for protons and neutrons, with deformation of the neutron density being more pronounced. This increased neutron deformation implies that valence neutrons have a key role in promoting quadrupole collectivity. The enhanced binding energy shown in Table 1 supports the extra energy linked to stable collective deformation [34,35].

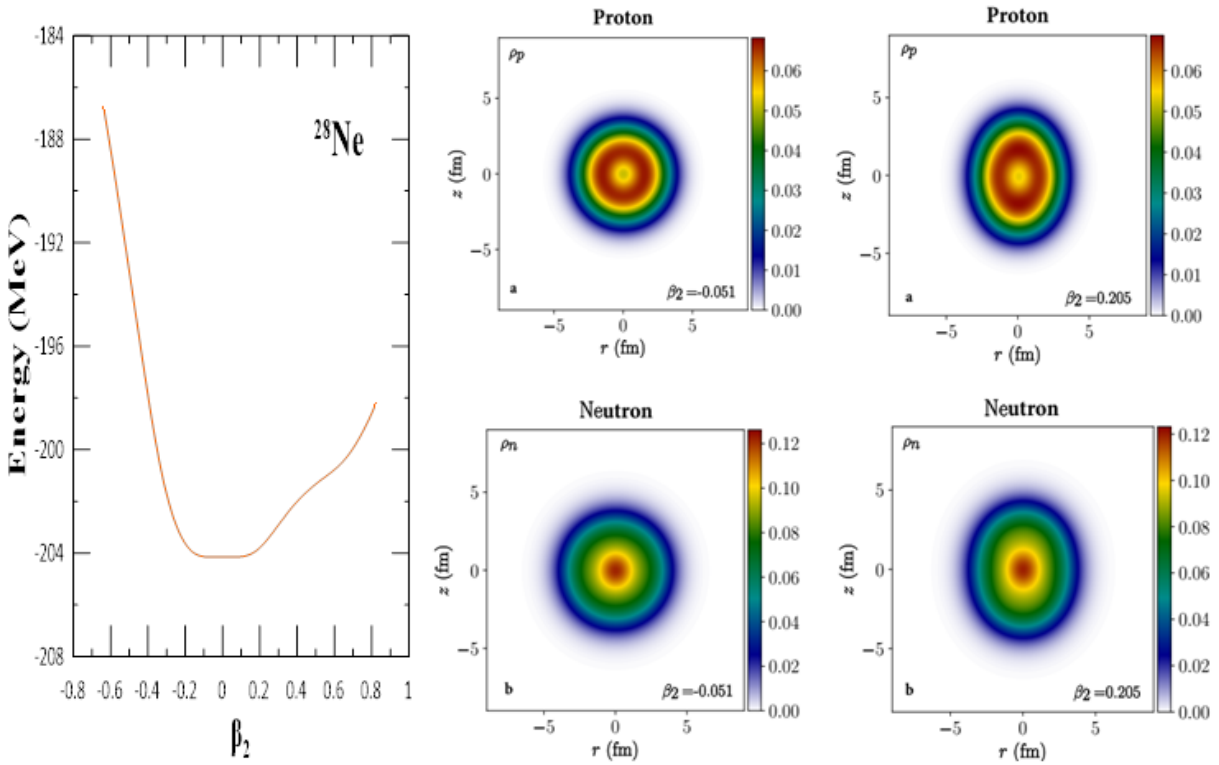

Figure 4 Left panel: PECs of ^{28}Ne as β_2. proton and neutron structure densities corresponding to the two local minima are shown on the right.

For ^{28}Ne, the PEC becomes notably flatter, and shows competing oblate and prolate minima in accordance with a very small equilibrium deformation $\beta_2 = -0.05$. The proton and neutron densities exhibit an almost similar shape with a slight deformation indicating a soft PES. The appearance of almost identical shapes suggests considerable mixing of configurations and transitions. The neutron density again exhibits somewhat greater deformation than the proton density, demonstrating the influence of neutron correlations around the $N = 20$ region. This softness is evident in the slight rise in binding energy compared with ^{26}Ne [36,37].

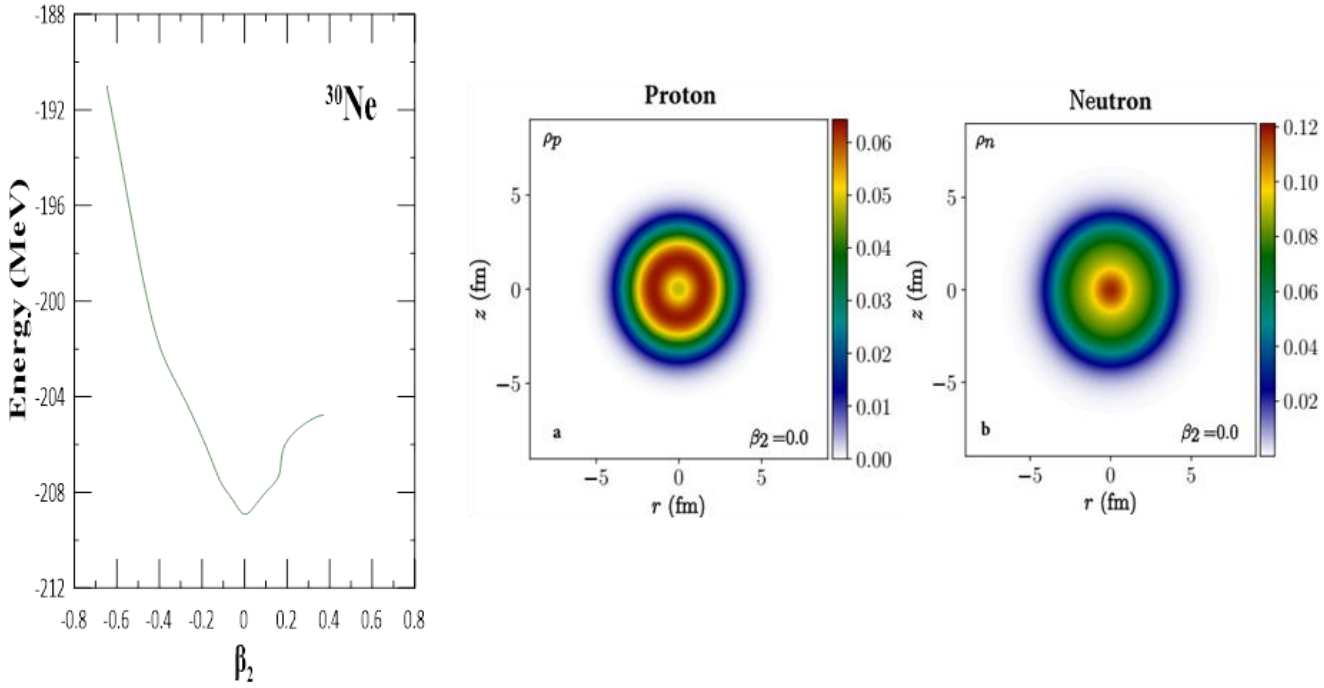

Figure 5 Left panel: PECs of ^{30}Ne as β_2. proton and neutron structure densities corresponding to the one local minimum are shown on the right.

In ^{30}Ne, the PEC minimum is located at $\beta_2 = 0$, fully consistent with the spherical equilibrium value reported in Table 1. Both the proton and neutron density distributions are nearly perfectly spherical, indicating a restoration of shell stabilization that suppresses quadrupole collectivity. The higher binding energy reflects the enhanced stability associated with this near-spherical configuration within the HF+BCS framework.

Table 1 Comparison of current β_2 and binding energy (BE) for Ne isotopes.

Nucleus	β_2 equilibrium (present work)	β_2 equilibrium [26]	BE, MeV (present work)	BE, MeV [26]	BE, Exp MeV [27]
^{24}Ne	−0.051	-0.063	187.037	192.61	191.843
^{26}Ne	0.102	0.121	199.691	202.25	201.605 ± 0.032
^{28}Ne	−0.051	-0.021	204.154	208.55	206.938 ± 0.161
^{30}Ne	0.000	0.000	208.911	212.44	211.221 ± 0.644

Table 1 reports the equilibrium deformation parameters and binding energies of the PECs and density distribution deformation trends. The small deformation of ^{24}Ne implies a small increase in binding energy and a small deformation-correlation effect. The steady prolate deformation of ^{26}Ne is associated with a binding energy increase, which substantiates that the quadrupole collectivity is a potent deflation mechanism. ^{28}Ne's binding energies, on the other hand, continue increasing without any apparent deformation. This illustrates the significant role of shape and dynamic correlations in nuclear stability. For ^{30}Ne, the spherical equilibrium configuration corresponds to the highest binding energy

along the isotopic chain, confirming the dominance of shell stabilization and suggesting a partial restoration of $N = 20$ shell closure. The earlier theoretical estimates and experimental data are found to be in good agreement for binding energy. The major differences are due to known limitations of HF+BCS, in particular simple pairing correlations and neglect of more advanced (MF) effects, like configuration mixing and symmetry restoration. The framework captures the essential characteristics of the neutron-rich Ne isotopes systematics and the deformation and binding energy evolution of Ne isotopes successfully.

4. CONCLUSIONS

The systematic analysis of deformation properties of even-even isotopes $^{24\text{-}30}$Ne is studied within the HF+BCS scheme using the Skyrme energy-density functional (SLy5). The findings regarding the potential energy curves collated with density distributions, binding energies, and trends suggests that the 24Ne nucleus has a soft and weakly deformed configuration and so does the ^{26}Ne where prolate deformation is stabilised. ^{28}Ne displays strong shape coexistence, and finally, ^{30}Ne reverts to a near-spherical configuration. The delicate interplay between quadrupole correlations and the shell effects near the ($N = 20$) region likely explains the deformation trend reflections for the isotopes. As neutron of number increases in the even-even neon isotopes, the structural evolution occurs distinctly as per the axially constrained HF+BCS calculation. Based on the results, it appears that the balance between shell effects and quadrupole interactions is changing relatively slowly, producing large changes in the shapes and stability of the nuclei. A reduced number of neutrons favors shell effects, leading to soft potential energy surfaces and dynamic, weak deformation upon additional neutron enrichment. The interplay between collective correlations and shell stabilization gives rise to transitional behavior characterized by shape softness and configuration mixing. The calculated BE are in good agreement with experimental trends, thus confirming HF+BCS method well represents total nuclear stability. As indicated by the systematic development of energy surfaces and density distributions, the current method is capable of reproducing the essential physics of nuclear shape evolution in neutron-rich systems. Although further beyond (MF) correlations could enhance its quantitative precision, the current framework provides a solid and clear physical interpretation of the structural modifications caused by an increase in neutron number.

References

[1] A. Kh. Shihab, A. H. Al-Mashhadani, R. M. Shalaby, Experimental and Theoretical NANOTECHNOLOGY, 10 (2026) 207. https://doi.org/10.56053/10.S.207
[2] O. Sorlin, M.-G. Porquet, Progress in Particle and Nuclear Physics, 61 (2008) 602. https://doi.org/10.1016/j.ppnp.2008.05.001
[3] M. Stoitsov, J. Dobaczewski, W. Nazarewicz, P. Ring, Computer Physics Communications, 167 (2005) 43. https://doi.org/10.1016/j.cpc.2004.12.010
[4] S. H. Mohammed, H. A. J. Hussein, Z. K. Nasser Allah, VII International Rimar Congress of Pure and Applied Sciences (2025) 19. https://doi.org/10.47832/RimarCongress07-3
[5] S. Ebata, T. Nakatsukasa, Physica Scripta, 92 (2017) 064005. https://doi.org/10.1088/1402-4896/aa6c19
[6] P. Ring, P. Schuck, The Nuclear Many-Body Problem, Springer-Verlag, Berlin (2004). https://doi.org/10.1007/978-3-540-21206-5
[7] D. Kherifi, A. Keziz, M. Rasheed, A. Oueslati, Ceramics International, 50 (2024) 1. https://doi.org/10.1016/j.ceramint.2024.05.317
[8] A. Zubaidi, L. M. Asaad, I. Alshalal, M. Rasheed, Journal of the Mechanical Behavior of Materials,

32 (2023) 1. https://doi.org/10.1515/jmbm-2022-0302
[9] M. Bender, P.-H. Heenen, P.-G. Reinhard, Reviews of Modern Physics, 75 (2003) 121. https://doi.org/10.1103/RevModPhys.75.121
[10] P.-G. Reinhard, W. Nazarewicz, Physical Review C, 87 (2013) 014324. https://doi.org/10.1103/PhysRevC.87.014324
[11] S. H. Mohammed, H. A. J. Hussein, M. G. Jasim, Z. A. Abbas, Experimental and Theoretical NANOTECHNOLOGY, 10 (2026) 517. https://doi.org/10.56053/10.2.517
[12] A. A. Alzubadi, R. T. Mahdi, Nuclear Physics and Atomic Energy, 26 (2025) 113. https://doi.org/10.15407/jnpae2025.02.113
[13] A. A. Alzubadi, R. T. Mahdi, Iraqi Journal of Physics, 23 (2025) 24. https://doi.org/10.30723/ijp.v23i3.1383
[14] Y. Utsuno, T. Otsuka, T. Mizusaki, M. Honma, Physical Review C, 60 (1999) 054315. https://doi.org/10.1103/PhysRevC.60.054315
[15] S. H. Mohammed, A. R. Ridha, Iraqi Journal of Physics, 16 (2018) 103. https://doi.org/10.20723/ijp.16.39.103-116
[16] S. H. Mohammed, A. R. Ridha, Iraqi Journal of Science, 59 (2018) 1866. https://doi.org/10.24996/ijs.2018.59.4A.12
[17] A. A. Alzubadi, R. A. Allawi, Indian Journal of Physics, 96 (2021) 1205. https://doi.org/10.1007/s12648-021-02052-x
[18] A. A. Alzubadi, Indian Journal of Physics, 89 (2014) 619. https://doi.org/10.1007/s12648-014-0614-3
[19] P.-G. Reinhard, B. Schuetrumpf, J. A. Maruhn, Computer Physics Communications, 258 (2020) 107603. https://doi.org/10.1016/j.cpc.2020.107603
[20] R. J. Furnstahl, K. Hebeler, Reports on Progress in Physics, 76 (2013) 126301. https://doi.org/10.1088/0034-4885/76/12/126301
[21] A. Jaber, M. Ismael, T. Rashid, M. A. Sarhan, M. Rasheed, I. M. Sala, Eureka: Physics and Engineering, 4 (2023) 29. https://doi.org/10.21303/2461-4262.2023.002770
[22] R. A. Broglia, V. Zelevinsky, Fifty Years of Nuclear BCS Pairing in Finite Systems, World Scientific, Singapore (2013). https://doi.org/10.1142/8716
[23] J. Erler, P. Klüpfel, P.-G. Reinhard, Journal of Physics G: Nuclear and Particle Physics, 37 (2010) 064001. https://doi.org/10.1088/0954-3899/37/6/064001
[24] W. Greiner, J. A. Maruhn, Nuclear Models, Springer-Verlag, New York (1996). https://doi.org/10.1007/978-1-4612-4214-8
[25] E. Kadri, et al., Journal of Alloys and Compounds, 705 (2017) 708. https://doi.org/10.1016/j.jallcom.2017.02.117
[26] P. Möller, A. J. Sierk, T. Ichikawa, H. Sagawa, Atomic Data and Nuclear Data Tables, 109–110 (2016) 1. https://doi.org/10.1016/j.adt.2016.04.006
[27] O. Alabdali, A. Guessab, Filomat, 34 (2020) 601. https://doi.org/10.2298/FIL2002601A
[28] A. I. A. Ali, M. RASHEED, Experimental and Theoretical NANOTECHNOLOGY, 10 (2026) 277. https://doi.org/10.56053/10.S.277
[29] A. Khaleefah, M. RASHEED, Experimental and Theoretical NANOTECHNOLOGY, 10 (2026) 289. https://doi.org/10.56053/10.S.289
[30] Z. S. Ahmed, M. RASHEED, H. S. Ahmed, Experimental and Theoretical NANOTECHNOLOGY, 10 (2026) 329. https://doi.org/10.56053/10.S.329
[31] Z. S. Ahmed, M. RASHEED, H. S. Ahmed, Experimental and Theoretical NANOTECHNOLOGY, 10 (2026) 343. https://doi.org/10.56053/10.S.343
[32] M. Rasheed, et al., Journal of Advanced Biotechnology and Experimental Therapeutics, 6 (2023) 495. https://doi.org/10.5455/jabet.2023.d144

[33] M. Rasheed, O. Y. Mohammed, S. Shihab, A. Al-Adili, Journal of Physics: Conference Series, 1795 (2021) 012042. https://doi.org/10.1088/1742-6596/1795/1/012042
[34] M. Enneffati, B. Louati, K. Guidara, M. Rasheed, R. Barillé, Journal of Materials Science: Materials in Electronics, 29 (2018) 171. https://doi.org/10.1007/s10854-017-7901-7
[35] A. J. Hussein, M. N. Al-Darraji, M. Rasheed, M. A. Sarhan, IOP Conference Series: Earth and Environmental Science, 1262 (2023) 022005. https://doi.org/10.1088/1755-1315/1262/2/022005
[36] M. Enneffati, M. Rasheed, B. Louati, K. Guidara, R. Barillé, Optical and Quantum Electronics, 51 (2019) 1. https://doi.org/10.1007/s11082-019-2015-5
[37] A. A. Abdulrahman, M. Rasheed, S. Shihab, Journal of Physics: Conference Series, 1879 (2021) 022118. https://doi.org/10.1088/1742-6596/1879/2/022118